

Simulation of Flagellated Bacteria Near a Solid Surface: Effects of Flagellar Morphology and Ionic Strength

Baopi Liu,¹ Bowen Jin,^{2,3} and Ning An⁴

¹Complex Systems Division, Beijing Computational Science Research Center, Beijing 100193, China

²Huanjiang Laboratory, Zhuji, Zhejiang 311899, China

³State Key Laboratory of Fluid Power and Mechatronic Systems, Department of Mechanics, Zhejiang University, Hangzhou, Zhejiang 310027, China

⁴School of Physics and Astronomy, Beijing Normal University, Beijing 100875, China

(*Electronic mail: bpliu@mail.bnu.edu.cn)

(Dated: 25 June 2025)

This study systematically investigates the dynamics of the bacterial transition from free-swimming to surface adhesion, a process characterized by both height h and inclination angle Ψ . The surface entrapment process is divided into three main stages. Initially, bacteria swim towards the surface at an approach velocity proportional to the motor rotation frequency. Subsequently, during the reorientation stage, the cotangent of the inclination angle decays exponentially with the product of the motor rotation frequency and time. Finally, the combined effect of near-field hydrodynamic interactions and DLVO forces drives the bacteria to a stable fixed point (h^*, Ψ^*) near the surface. Bacteria with left-handed chiral flagella exhibit clockwise circular motion on the surface. The stable height, inclination angle, and radius of curvature of these circular trajectories are collectively determined by the flagellar morphology and ionic strength of the electrolyte solution. More precisely, increasing the contour length of the flagellum decreases the stable inclination angle and increases the radius of curvature. In contrast, decreasing the ionic strength increases the stable height and radius of curvature, while also decreasing the stable inclination angle. Typically, the stable inclination angle falls within $(\pi/2, \pi)$, the stable height ranges from a few nanometers to approximately one hundred nanometers, and the radius of curvature of the circular motion spans several to tens of micrometers.

I. INTRODUCTION

Bacteria typically swim in fluid media by generating propulsion through flagellar rotation^{1,2}. Near the surfaces, the interactions between bacteria and the solid-liquid interface are significantly influenced by boundary conditions, which determine the slip velocity at the interface. These boundary conditions can be classified into three categories: no-slip, partial-slip, and perfect-slip³. They play an essential role in surface interactions and bacterial motility, affecting processes such as bacterial adhesion and the formation of biofilms, which are complex communities of bacteria embedded in an extracellular polymeric substance matrix⁴. The formation of biofilms is closely associated with numerous infectious diseases and contamination of medical devices⁴⁻⁸. Consequently, a comprehensive understanding and controlled manipulation of biofilm formation are crucial for diverse applications, including wastewater treatment⁹, bioremediation¹⁰, and biomedical engineering^{11,12}.

Understanding the dynamics of bacteria near surfaces is fundamental for various biological and engineering processes¹³⁻¹⁶. In recent decades, extensive experimental, numerical, and analytical studies have greatly advanced our understanding of bacterial dynamics near surfaces of various properties¹⁷⁻²³. Experimental observations suggest that bacterial surface entrapment typically involves three main stages: approach, reorientation, and surface swimming²⁴⁻²⁶. However, hydrodynamic interactions alone are not sufficient to account for the stable swimming behaviors observed in bacteria near solid surfaces^{27,28}. In addition to hydrodynamic interactions, van der Waals and electrostatic interactions, as de-

scribed by the Derjaguin–Landau–Verwey–Overbeek (DLVO) theory, also play a significant role in bacterial behavior near surfaces^{27,29-34}. Specifically, van der Waals forces typically dominate at larger separation distances, while electrostatic forces become increasingly prominent at shorter distances^{35,36}. The stable separation distance between bacteria and surfaces is estimated to range from approximately 4.25 – 140 nm²¹, with the radius of curvature of circular trajectories increasing correspondingly with the surface separation distance²⁸.

Under the no-slip boundary condition, the tangential component of the fluid velocity at the interface is equal to that of the surface³. Consequently, as bacteria swim near these surfaces, the shear forces within the flows exert a torque on them, leading to the orientation of their cell bodies towards the surface²⁴. However, the flagella resist this rotation³⁷. Under the combined influence of hydrodynamic forces acting on the cell body and flagellum, as well as electrostatic and van der Waals interactions described by DLVO theory, bacteria reach a stable fixed point. This point is characterized by a specific height above the surface and an inclination angle^{32,38}. DLVO theory can be used to describe how the ionic strength affects the stable swimming behavior of bacteria on surfaces. The Debye length, a critical parameter in this theory, is highly sensitive to the ionic strength of the electrolyte solution^{27,32,35,36,39}. Furthermore, the flagellar morphology of bacteria markedly influences their motility patterns on surfaces^{38,40,41}, including properties such as the radius of curvature of the circular motion observed in experiments. These radii are typically in the range of 8 – 50 μm ^{27,29,38,40-42}. However, the underlying mechanisms by which the bacterial flagellar morphology and

the ionic strength of the electrolyte solution collaboratively determine the stable height, inclination angle, and radius of curvature of bacterial circular motion remain unclear.

Monotrichous bacteria, which possess only a single helical flagellum, are particularly suitable for simulation modeling due to their simple morphology^{32,38,43,44}. To systematically explore the influence of flagellar morphology and the ionic strength of the electrolyte solution on the stable swimming behavior of bacteria near a solid surface, we develop a mathematical model of a bacterium with a rigid helical flagellum swimming near a solid surface. A detailed description of this modeling framework and the numerical simulation methods is provided in Sec. II. A, and the DLVO theory is presented in Sec. II. B. First, we examine the three main stages of the bacterial surface entrapment in Sec. III. A. Subsequently, Secs. III. B and III. C investigate the stable fixed point and the radius of curvature of the stable circular motion, respectively. Finally, the main conclusions are summarized in Sec. IV.

II. MODEL AND METHODS

A. Bacterial Model

Bacteria swimming in a fluid medium are in the low Reynolds number regime (typically $Re \approx 10^{-4}$), in which the dynamics is described by the incompressible Stokes equations. The viscous forces and torques for various parts of the flagellated bacteria are linearly related to their translational and rotational velocities. Specifically, these relationships are expressed as^{42,45,46}

$$\begin{pmatrix} \mathbf{F}_b \\ \mathbf{T}_b \\ \mathbf{F}_t \\ \mathbf{T}_t \end{pmatrix} = \mathcal{R} \begin{pmatrix} \mathbf{U}_b \\ \mathbf{W}_b \\ \mathbf{U}_t \\ \mathbf{W}_t \end{pmatrix}. \quad (1)$$

where \mathbf{U}_b and \mathbf{W}_b are the instantaneous translational and rotational velocities of the cell body, while \mathbf{U}_t and \mathbf{W}_t represent the instantaneous translational and rotational velocities of the flagellum, respectively. \mathbf{F}_b , \mathbf{T}_b , \mathbf{F}_t , and \mathbf{T}_t are the forces and torques exerted on the fluid by the cell body and the flagellum, respectively. In this study, the bacterial model consists of a spherical cell body and a rigid helical flagellum, as illustrated in Fig. 1. The connection point between the flagellar axis and the surface of the cell body is defined as \mathbf{r}_0 . In the laboratory coordinate system, the centerline positions of the left-handed helical flagellum are given by⁴⁷:

$$\mathbf{r}(s) = s \cos \theta \mathbf{D}_1 + R \sin \phi \mathbf{D}_2 + R \cos \phi \mathbf{D}_3 + \mathbf{r}_0. \quad (2)$$

where $\phi = ks \cos \theta$ is the phase and $k = 2\pi/\lambda$ is the wave number. The parameter $s \in [0, \Lambda]$ is a variable along the flagellar centerline, measured from the point \mathbf{r}_0 .

We consider separately the resistance matrices of the cell body and the flagellum, neglecting both the hydrodynamic interactions between them²⁸ and those between the flagellum and the surface. The cross-sectional radius of the flagellum is approximately 10 nm⁴⁸, and the hydrodynamic interactions

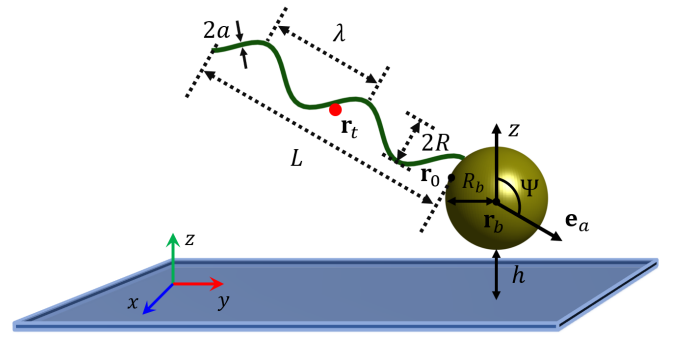


FIG. 1. Illustration of a bacterium near a solid surface. The height h represents the distance between the surface of the cell body and the solid surface. The inclination angle Ψ is defined as the angle between the direction of the flagellar axis and the z -axis. The radius of the cell body is R_b , the flagellar axis length is L , the helix radius is R , the filament radius is a , and the centers of the cell body and flagellum are \mathbf{r}_b and \mathbf{r}_t , respectively.

between the flagellum and the surface become significant only at separations less than the filament radius³⁹. Since, in non-colonizing bacteria, the separation between the flagellum and the surface rarely approaches below this value, these interactions can be reasonably neglected¹¹. Consequently, the resistance matrix \mathcal{R} of the bacterial system can be expressed as

$$\mathcal{R} = \begin{pmatrix} \mathcal{R}_b & 0 \\ 0 & \mathcal{R}_t \end{pmatrix}. \quad (3)$$

where \mathcal{R}_b and \mathcal{R}_t are the resistance matrices of the cell body and the flagellum, respectively. As shown in Fig. 1, consider a bacterium swimming near a solid surface. The resistance matrix \mathcal{R}_b of the spherical cell body is given by⁴²:

$$\mathcal{R}_b = \begin{pmatrix} Y_{\parallel}^A & 0 & 0 & 0 & Y^B & 0 \\ 0 & Y_{\parallel}^A & 0 & -Y^B & 0 & 0 \\ 0 & 0 & Y_{\perp}^A & 0 & 0 & 0 \\ 0 & -Y^B & 0 & Y_{\parallel}^C & 0 & 0 \\ Y^B & 0 & 0 & 0 & Y_{\parallel}^C & 0 \\ 0 & 0 & 0 & 0 & 0 & Y_{\perp}^C \end{pmatrix}. \quad (4)$$

The detailed expressions of Y_{\parallel}^A , Y_{\perp}^A , Y^B , Y_{\parallel}^C , and Y_{\perp}^C , which represent the translational and rotational resistance coefficients of the cell body in directions parallel and perpendicular to the surface, are presented in Appendix B. Note that Eq. 1, which describes the motion of bacteria near a solid surface, forms a system of nonlinear equations.

The helical flagellum is simplified as a chiral body, and its 6×6 resistance matrix, \mathcal{R}_t , can be calculated using RFT^{49–51}. The matrix is expressed as follows^{52,53}:

$$\mathcal{R}_t = \begin{pmatrix} A^f & B^f \\ B^f & C^f \end{pmatrix}. \quad (5)$$

where the submatrices of the flagellar resistance matrix are

TABLE I. Symbols, definitions and values in the present simulation.

Notation	Description	Value
μ	Dynamic viscosity	$1.0 \mu\text{g}/(\mu\text{m}\cdot\text{s})$
R_b	Radius of cell body	$1.0 \mu\text{m}$
R	Helix radius	$0.25 \mu\text{m}$
a	Filament radius	$0.01 \mu\text{m}$
θ	Pitch angle	$\pi/5$
f	Motor rotation rate	100 Hz
\mathbf{e}_a	Flagellar axis direction	y-axis
\mathbf{e}_m	Rotation direction of motor	$\mathbf{e}_m = \frac{\mathbf{r}_0 - \mathbf{r}_b}{ \mathbf{r}_0 - \mathbf{r}_b }$
h	Height above the surface	
Ψ	inclination angle	$0 \sim \pi$

defined as:

$$\begin{aligned} A^f &= X_{\parallel}^A \mathbf{e}_a \otimes \mathbf{e}_a + X_{\perp}^A (\mathbb{I} - \mathbf{e}_a \otimes \mathbf{e}_a), \\ B^f &= X_{\parallel}^B \mathbf{e}_a \otimes \mathbf{e}_a + X_{\perp}^B (\mathbb{I} - \mathbf{e}_a \otimes \mathbf{e}_a), \\ C^f &= X_{\parallel}^C \mathbf{e}_a \otimes \mathbf{e}_a + X_{\perp}^C (\mathbb{I} - \mathbf{e}_a \otimes \mathbf{e}_a). \end{aligned} \quad (6)$$

where \mathbf{e}_a denotes the unit vector along the axial direction of the flagellum, with the superscript "f" indicating the flagellum. The detailed expressions for X_{\parallel}^A , X_{\perp}^A , X_{\parallel}^B , X_{\perp}^B , X_{\parallel}^C , and X_{\perp}^C are provided in Appendix C.

The instantaneous translational and rotational velocities of the cell body are defined as $\mathbf{U}_b = (U_x, U_y, U_z)$ and $\mathbf{W}_b = (W_x, W_y, W_z)$, respectively. The corresponding velocities of the flagellar center are given by:

$$\begin{aligned} \mathbf{W}_t &= \mathbf{W}_b + \mathbf{W}_0, \\ \mathbf{U}_t &= \mathbf{U}_b + \mathbf{W}_t \times (\mathbf{r}_t - \mathbf{r}_b). \end{aligned} \quad (7)$$

where $\mathbf{W}_0 = 2\pi f \mathbf{e}_m$ is the rotational velocity of the motor, and \mathbf{r}_b , \mathbf{r}_t are the positions of the centers of the cell body and the flagellum, respectively, with the distance between them given by $l = L/2 + R_b$. The bacterial model can be simplified to a chiral two-body model^{52,53}. For a bacterium swimming near a solid surface, the force and torque balance conditions are:

$$\begin{aligned} \mathbf{F}_b + \mathbf{F}_t - \mathbf{F}_b^{ext} - \mathbf{F}_t^{ext} &= 0, \\ \mathbf{T}_b + \mathbf{T}_t - \mathbf{T}_b^{ext} - \mathbf{T}_t^{ext} + (\mathbf{r}_t - \mathbf{r}_b) \times (\mathbf{F}_t - \mathbf{F}_t^{ext}) &= 0. \end{aligned} \quad (8)$$

where \mathbf{F}_b^{ext} , \mathbf{T}_b^{ext} , \mathbf{F}_t^{ext} , and \mathbf{T}_t^{ext} are external forces and torques exerted on the cell body and flagellum, respectively, excluding hydrodynamic forces and torques.

The parameters and their values used in our simulations are listed in Table I.

B. DLVO Theory

The bacterium is simplified as a model comprising a spherical cell body and a rigid helical flagellum. When bacteria swim near a solid surface, the interactions between the cell body and the surface include hydrodynamic forces, van der Waals forces, and electrostatic forces. The latter two interactions are described by the DLVO theory^{4,11,30-32}. According

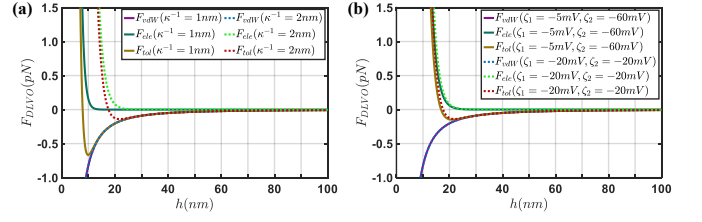


FIG. 2. DLVO force as a function of separation distance h between a spherical cell body and a solid surface. (a) DLVO force for different Debye lengths, with $\zeta_1 = -20 \text{ mV}$ and $\zeta_2 = -20 \text{ mV}$. (b) DLVO force for different zeta potentials, with $\kappa^{-1} = 2 \text{ nm}$.

to DLVO theory, the total interaction force, F_D , between the cell body and the surface is the sum of the attractive van der Waals (vdW) force and the repulsive or attractive electrostatic (ele) force:

$$F_D(h) = F_{vdW}(h) + F_{ele}(h). \quad (9)$$

where h represents the separation distance between the cell body and the solid surface. The subscripts denote different types of interactions. The mathematical expressions for these interaction energies are given as follows^{35,36}:

$$\begin{aligned} G_{vdW}(h) &= -\frac{H}{12} \left[\frac{2R_b(h+R_b)}{h(h+2R_b)} + \ln \left(\frac{h}{h+2R_b} \right) \right], \\ G_{ele}(h) &= \pi \epsilon R_b \left[2\zeta_1 \zeta_2 \ln \left(\frac{1+e^{-\kappa h}}{1-e^{-\kappa h}} \right) \right. \\ &\quad \left. + (\zeta_1^2 + \zeta_2^2) \ln \left(1 - e^{-2\kappa h} \right) \right]. \end{aligned} \quad (10)$$

The corresponding forces are obtained by differentiation:

$$\begin{aligned} F_{vdW}(h) &\equiv -\frac{\partial G_{vdW}(h)}{\partial h} = -\frac{H}{3} \frac{R_b^3}{h^2(h+2R_b)^3}, \\ F_{ele}(h) &\equiv -\frac{\partial G_{ele}(h)}{\partial h} = 2\pi \epsilon \kappa R_b \frac{2\zeta_1 \zeta_2 e^{\kappa h} - (\zeta_1^2 + \zeta_2^2)}{e^{2\kappa h} - 1}. \end{aligned} \quad (11)$$

where R_b is the radius of the cell body, H is the Hamaker constant, and ζ_1 and ζ_2 are the zeta potentials of the cell body surface and the solid surface, respectively. Typical zeta potential values are shown in Table II. The inverse Debye length, κ , is given by^{36,39}

$$\kappa^{-1} = \sqrt{\frac{\epsilon k_B T}{2e^2 N_A I}} \approx \frac{0.304}{\sqrt{I}} \text{ nm}. \quad (12)$$

where $\epsilon = 6.933 \times 10^{-10} \text{ C}^2/(\text{N}\cdot\text{m}^2)$ is the permittivity of water at room temperature $T = 298 \text{ K}$, $k_B = 1.381 \times 10^{-23} \text{ J/K}$ is the Boltzmann constant, $e = 1.602 \times 10^{-19} \text{ C}$ is the elementary charge, $N_A = 6.022 \times 10^{23} \text{ mol}^{-1}$ is the Avogadro constant and I is the ionic strength in mol/L (or M). Typical values of ionic strength and zeta potential are listed in Table II. Eq. 12 indicates that lower ionic strengths correspond to larger Debye lengths.

TABLE II. Typical values of Debye length corresponding to different ionic strength I at 298 K. Zeta potentials for various bacteria and surface.

I (mol/L)	κ^{-1} (nm)	ζ_1 (Bacterium) (mV)	ζ_2 (Surface) (mV)
0.006	3.92	-22.82	-37.29 ²⁹
0.006	3.92	-25.1	-56.8 ³¹
0.01	3.04	-30 ± 1	-21 ± 2 ³⁴
0.01	3.04	-53 ± 2	-21 ± 2 ³⁴
0.024	2.00	-20.0	-20.0 ³²
0.05	1.36	-14 ± 2	-12 ± 1 ³⁴
0.05	1.36	-43 ± 2	-12 ± 1 ³⁴
0.1	0.96	-11 ± 1	-8 ± 1 ³⁴
0.1	0.96	-36 ± 3	-8 ± 1 ³⁴
0.19	0.697	-21.5	-36.2 ²⁷
0.20	0.680	-19.6	-18.7 ³¹
0.202	0.676	-4.77	-14.29 ²⁹

The Hamaker constant H typically ranges from 10^{-21} J to 10^{-19} J. In this work, we fix the values to be $H = 10^{-21}$ J, consistent with previous studies^{27,32}. Fig. 2 presents the DLVO force profiles for different Debye lengths κ^{-1} and zeta potentials ζ_1 and ζ_2 . The left panel of Fig. 2 illustrates the van der Waals and electrostatic forces for $\zeta_1 = -20$ mV and $\zeta_2 = -20$ mV, with Debye lengths of $\kappa^{-1} = 1$ nm and $\kappa^{-1} = 2$ nm. The right panel of Fig. 2 shows the corresponding forces for different zeta potentials, with a fixed Debye length of $\kappa^{-1} = 2$ nm. A comparison between the two panels in Fig. 2 reveals that the DLVO force is sensitive to changes in Debye length but insensitive to changes in the zeta potential. Therefore, we set $\zeta_1 = \zeta_2 = -20$ mV and focus mainly on investigating the effects of the Debye length κ^{-1} on bacterial motility near a solid surface.

III. RESULTS

A. Three Stages of Surface Entrapment

The trajectory of swimming bacteria is determined by their initial positions and orientations. It is impractical to perform long simulations for all possible initial conditions to explore the complete picture. The height h above the surface and the inclination angle Ψ effectively simplify the analysis of the bacterial dynamics near a solid surface. Moreover, phase averaging further eliminates the effects of the flagellar phase, as it is a variable that changes rapidly^{38,40}. Singly flagellated bacteria can be approximated using a chiral two-body model, which is obtained by integrating the centerline of the flagellum using RFT⁵²⁻⁵⁴. Neglecting Brownian motion, bacterial trajectories near the surface are simulated using Eq. 1. Specifically, the center position of the cell body is updated iteratively as follows⁴⁷:

$$\mathbf{r}_b(t + \Delta t) = \mathbf{r}_b(t) + \mathbf{U}_b(t)\Delta t. \quad (13)$$

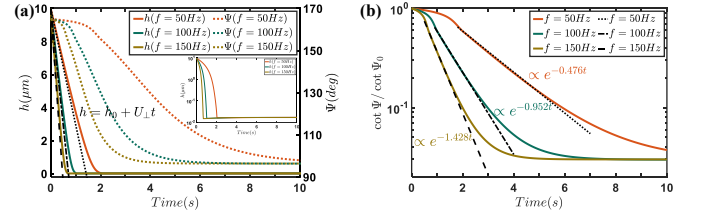


FIG. 3. (a) Time evolution of the surface distance h and inclination angle Ψ under different motor rotation frequencies. The inset shows the variation of height h over time. The dashed black lines represent the analytical solutions. (b) Time evolution of normalized cotangent of inclination angle $\cot \Psi / \cot \Psi_0$. The dashed black lines show the fitted results.

The axial direction of the flagellum, \mathbf{e}_a , is updated through rotation:

$$\mathbf{e}_a(t + \Delta t) = \mathbf{R}(\mathbf{e}_b, \theta_b) \cdot \mathbf{e}_a(t). \quad (14)$$

where $\mathbf{e}_b = \mathbf{W}_b / |\mathbf{W}_b|$ is the unit vector along the rotation axis of the cell body, and $\theta_b = |\mathbf{W}_b| \Delta t$ is the rotation angle of the cell body. The rotation matrix $\mathbf{R}(\mathbf{e}, \theta)$ is Rodrigues' rotation matrix, defined as^{47,55,56}

$$\mathbf{R}(\mathbf{e}, \theta) = \cos \theta \mathbb{I} + (1 - \cos \theta) \mathbf{e} \otimes \mathbf{e}^T + \sin \theta \mathbf{e} \times. \quad (15)$$

where \mathbb{I} is a 3×3 identity matrix, \otimes denotes the Kronecker product, and $(\mathbf{e} \times)$ is a 3×3 antisymmetric matrix defined such that $(\mathbf{e} \times) \mathbf{v} = \mathbf{e} \times \mathbf{v}$ for any vector \mathbf{v} . The position of the flagellar center is updated as:

$$\mathbf{r}_f(t + \Delta t) = \mathbf{r}_b(t + \Delta t) - l \mathbf{e}_a(t + \Delta t). \quad (16)$$

Here, the motor rotation direction is aligned with the negative of the flagellar axial direction, that is, $\mathbf{e}_m = -\mathbf{e}_a$.

We use a Hamaker constant of $H = 10^{-21}$ J, zeta potentials of $\zeta_1 = \zeta_2 = -20$ mV, and a Debye length of $\kappa^{-1} = 2$ nm in our simulations. The bacterium is initially positioned at a height of $h_0 = 10 \mu\text{m}$ above the surface, with an initial inclination angle of $\Psi_0 = 165^\circ$. The time step interval is set to $\Delta t = 5 \times 10^{-4}$ s. The time evolutions of height h and inclination angle Ψ are shown in Fig. 3 (a) for various motor rotation frequencies. This process can be divided into three main stages: approach, reorientation, and surface swimming. The translational velocities parallel (\parallel) and perpendicular (\perp) to the xy -plane in the bulk fluid are given by⁵³

$$U_{\parallel} = \frac{8\pi\mu R_b^3 X_{\parallel}^B \cdot \sin \Psi}{(X_{\parallel}^B)^2 - (X_{\parallel}^A + 6\pi\mu R_b)(X_{\parallel}^C + 8\pi\mu R_b^3)} W_0, \quad (17)$$

$$U_{\perp} = \frac{8\pi\mu R_b^3 X_{\parallel}^B \cdot \cos \Psi}{(X_{\parallel}^B)^2 - (X_{\parallel}^A + 6\pi\mu R_b)(X_{\parallel}^C + 8\pi\mu R_b^3)} W_0.$$

where $W_0 = -2\pi f$ is the motor rotation rate, which implies that the flagellum rotates anticlockwise (when viewed from behind the bacterium). The black dashed lines in Fig. 3(a) represent the analytical solution $h = h_0 + U_{\perp} t$, indicating that

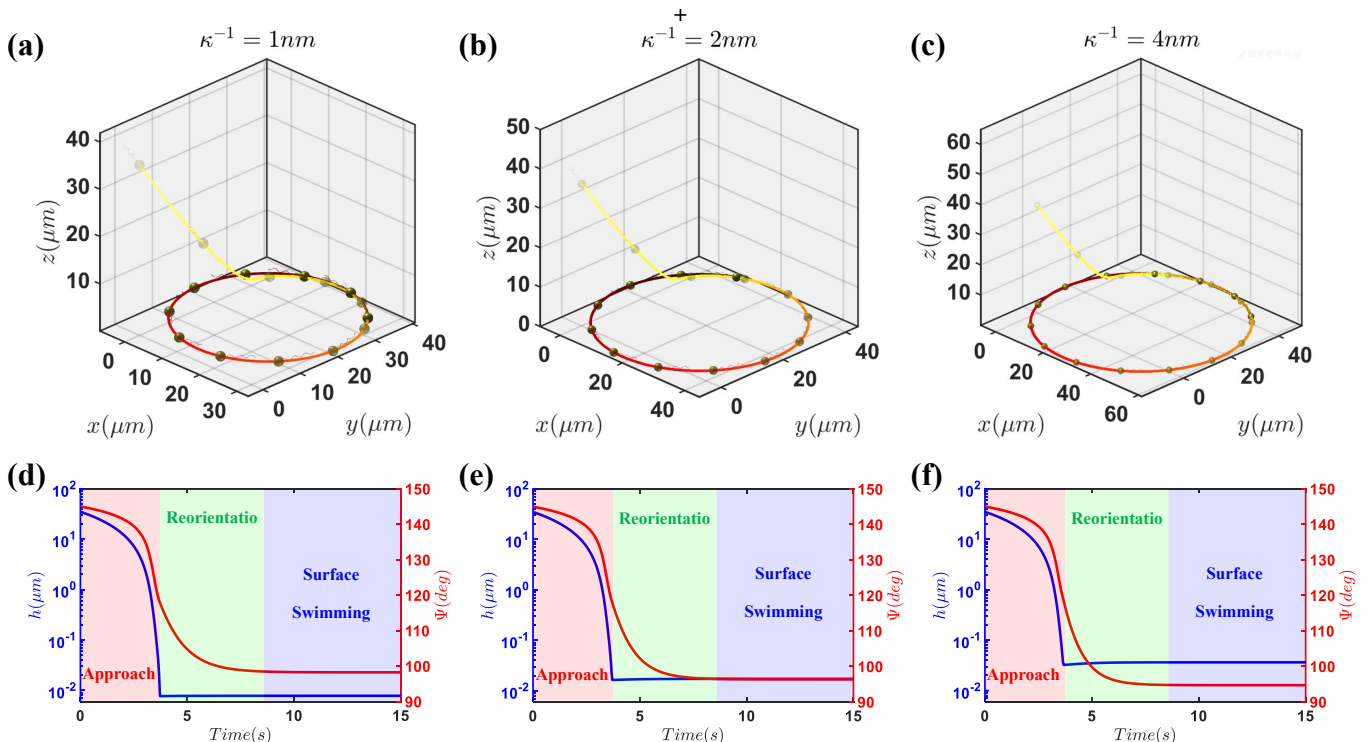


FIG. 4. Trajectories of a bacterium approaching a solid surface and exhibiting clockwise circular swimming are shown for different Debye lengths: (a) $\kappa^{-1} = 1 \text{ nm}$, (b) $\kappa^{-1} = 2 \text{ nm}$, and (c) $\kappa^{-1} = 4 \text{ nm}$, all starting from the same initial condition. The color of the trajectory lines gradually darkens over time. (d)(e)(f) The corresponding heights h (blue lines) and inclination angles Ψ (red lines), both as functions of time.

during the initial stage, bacteria exhibit quasi-linear motion with an approach velocity proportional to the motor rotation frequency.

During the reorientation stage, the bacterial height h remains approximately constant, while the inclination angle Ψ evolves over time, as shown in Fig. 3(a). The time evolution of $\cot \Psi$ is illustrated in Fig. 3(b). The motor rotation frequencies are set to $f = 50 \text{ Hz}$, $f = 100 \text{ Hz}$, and $f = 150 \text{ Hz}$, where Ψ_0 is the initial inclination angle. As observed in Fig. 3(b), the exponent in the exponential function is proportional to the motor rotation frequency f . The relationship between the inclination angle Ψ , the motor rotation frequency f and the time t can be approximated by $\cot \Psi / \cot \Psi_0 \propto e^{-\alpha f t}$, where α is a constant that depends on the bacterial morphology and the stable height h^* ²⁶.

When swimming parallel to the solid surface, the bacteria maintain a constant height h^* and an inclination angle Ψ^* . To clearly demonstrate the effect of the Debye length (that is, ionic strength) on the radius of curvature of the stable circular trajectory, we perform numerical simulations using several commonly used Debye lengths: $\kappa^{-1} = 1 \text{ nm}$ (corresponding to an ionic strength of $I \approx 0.1 \text{ M}$), $\kappa^{-1} = 2 \text{ nm}$ and $\kappa^{-1} = 4 \text{ nm}$ (corresponding to $I \approx 0.006 \text{ M}$), the detailed values are provided in Table II. In these simulations, shown in Fig. 4, the contour length of the flagellum is set to $\Lambda = 7.5 \mu\text{m}$, and the motor rotation frequency is $f = 100 \text{ Hz}$. The initial conditions are $h_0 = 35 \mu\text{m}$ and $\Psi_0 = 145^\circ$.

Figs. 4(a)-(c) illustrate the trajectories of a bacterium un-

der different Debye lengths, highlighting the clockwise circular swimming observed during the third stage. Figs. 4(d)-(f) depict the time evolution of the height and inclination angle, emphasizing these three main stages in bacterial motility. The radii of curvature of the stable circular trajectories are approximately $r \approx 19 \mu\text{m}$, $r \approx 25 \mu\text{m}$, and $r \approx 33 \mu\text{m}$ for Debye lengths $\kappa^{-1} = 1 \text{ nm}$, $\kappa^{-1} = 2 \text{ nm}$, and $\kappa^{-1} = 4 \text{ nm}$, respectively. Correspondingly, the stable heights are $h^* = 7.8 \text{ nm}$, $h^* = 17.2 \text{ nm}$, and $h^* = 36.4 \text{ nm}$, while the stable inclination angles are $\Psi^* = 98.2^\circ$, $\Psi^* = 96.4^\circ$, and $\Psi^* = 94.7^\circ$. These results indicate that increasing the Debye length (that is, decreasing the ionic strength) results in an increase in stable height, a smaller inclination angle, and a larger radius of curvature of the bacterial surface swimming trajectories.

B. Stable Fixed Point

The kinematic characteristics of a bacterium swimming near a solid surface are fully described by the height h above the surface and the inclination angle Ψ , which together define the phase plane (h, Ψ) . This phase plane offers a detailed characterization of bacterial motion near a solid surface. Previous studies have demonstrated the existence of a stable fixed point (h^*, Ψ^*) , which satisfies the following equations^{38,43}:

$$\begin{cases} \dot{h}(h^*, \Psi^*) = 0, \\ \dot{\Psi}(h^*, \Psi^*) = 0. \end{cases} \quad (18)$$

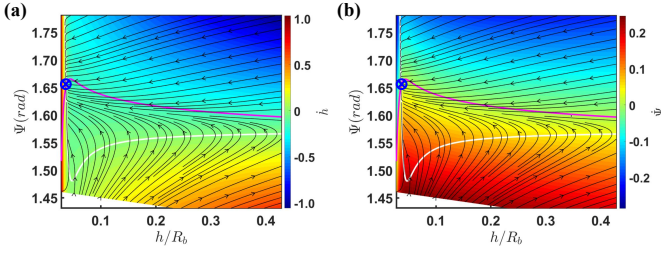


FIG. 5. Phase plane diagrams for a bacterium model near a solid surface. The contour length of the flagellum is $\Lambda = 7.50 \mu\text{m}$. The background color maps represent (a) the translational velocity \dot{h} and (b) the angular velocity $\dot{\Psi}$. The white and pink curves show where $\dot{h} = 0$ and $\dot{\Psi} = 0$, respectively. The symbol \otimes marks the stable fixed point.

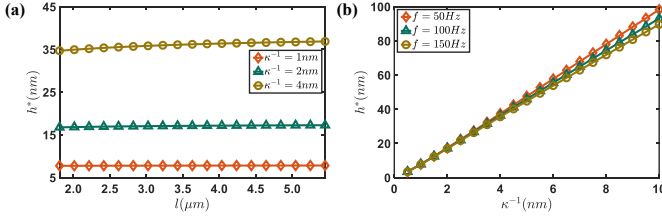


FIG. 6. Variation of the stable height h^* as functions of (a) the distance l and (b) the Debye length κ^{-1} , respectively.

In this section, we constrain the bacterial axis \mathbf{e}_a to the yz -plane, with the z -axis normal to the surface. Consequently, Eq. 18 simplifies to:

$$\begin{cases} U_z = 0, \\ W_x = 0. \end{cases} \quad (19)$$

The phase plane of a bacterium swimming near a solid surface is presented in Fig. 5. For this simulation, the flagellum has a contour length of $\Lambda = 7.5 \mu\text{m}$, and the Debye length is $\kappa^{-1} = 4.0 \text{ nm}$. The background color maps in Figs. 5(a) and (b) illustrate the values of \dot{h} and $\dot{\Psi}$, respectively. The white and pink curves the contours where $\dot{h} = 0$ and $\dot{\Psi} = 0$, respectively. The blank regions indicate areas that are physically inaccessible to the bacteria due to the presence of the solid surface. The figure clearly shows the existence of a unique stable fixed point (h^*, Ψ^*) in the phase plane, with no other fixed points observed. Consequently, once the bacterium reaches this stable fixed point, its height h and inclination angle Ψ remain constant.

As shown in Fig. 4, the ionic strength significantly influences the stable height, the stable inclination angle, and the radius of curvature of the stable circular trajectory near a solid surface. Experimental evidence also suggests that the radius of curvature depends on the stable height h^* ²⁸. In this section, we investigate how flagellar morphology and ionic strength affect stable height h^* , with results presented in Fig. 6. The stable height is relatively insensitive to the contour length of the flagellum, as shown in Fig. 6(a). This suggests that within the scope of this study the effect of flagellar contour length on stable height h^* can be considered negligible.

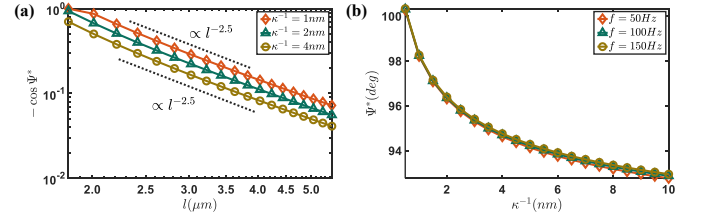


FIG. 7. (a) The negative cosine of the stable inclination angle, $-\cos \Psi^*$, as a function of the distance l . (b) The stable inclination angle, Ψ^* , as a function of Debye length κ^{-1} .

However, Fig. 6(b) demonstrates that the stable height h^* is highly sensitive to Debye length, increasing with it. In our simulations, the contour length of the flagellum is $\Lambda = 7.5 \mu\text{m}$. Under high ionic strength conditions ($I = 0.1 - 0.3 \text{ M}$)^{34,57}, h^* can be less than 10 nm. In contrast, under low ionic strength conditions ($I = 0.006 - 0.01 \text{ M}$)^{29,31,34}, h^* can reach approximately 100 nm. In general, the data in Fig. 6(b) indicate that h^* increases approximately linearly with the Debye length κ^{-1} .

In this section, we investigate the relationship between the stable inclination angle Ψ^* and the distance $l = L/2 + R_b$ as well as the Debye length κ^{-1} . As illustrated in Fig. 7, the stable inclination angle decreases as l increases. For sufficiently short flagella, bacteria tend to orient toward the surface ("nose down"), a phenomenon observed experimentally¹⁴. This occurs because shorter flagella produce weaker torques that are insufficient to counteract the rotation of the cell body^{21,22}. As the contour length of the flagellum increases, the stable inclination angle Ψ^* decreases correspondingly, approaching approximately $\Psi^* \approx 96^\circ$ for a flagellum with a contour length of $\Lambda = 7.5 \mu\text{m}$. The relationship between $-\cos \Psi^*$ and l follows an empirical power law $-\cos \Psi^* \propto l^{-2.5}$.

Fig. 7(b) illustrates the relationship between the stable inclination angle Ψ^* and the Debye length κ^{-1} for a flagellar contour length of $\Lambda = 7.5 \mu\text{m}$. As the Debye length κ^{-1} increases, the stable inclination angle decreases. Furthermore, the motor rotation frequency has a negligible effect on the stable inclination angle.

C. Radius of Curvature of the Circular Orbit

When a bacterium swims near a solid surface, the direction of its circular motion is determined by the chirality of its flagellum. Specifically, if the flagellum is a left-handed helix, the bacterium tends to exhibit a clockwise circular motion. The radius of curvature, r , of this circular trajectory is given by

$$r = \frac{U_{\parallel}}{|W_{\perp}|} = \frac{\sqrt{U_x^2 + U_y^2}}{|W_z - (W_x \cos \phi + W_y \sin \phi) \cot \Psi^*|} \quad (20)$$

where U_{\parallel} is the translational velocity component parallel to the surface, and W_{\perp} is the rotational velocity component perpendicular to the surface (along the z -axis). A detailed expression for the radius of curvature of the circular motion is

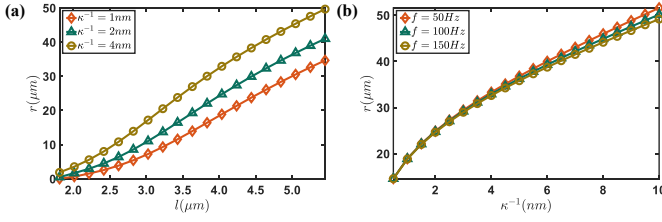


FIG. 8. The radii of curvature of the circular trajectory as functions of (a) the distance l and (b) the Debye length κ^{-1} .

provided in Appendix A. The radii of curvature, r , which depend on the distance l and the Debye length κ^{-1} , are shown in Fig. 8.

Fig. 8(a) illustrates that the radius of curvature, r , of circular trajectories increases with increasing distance l . Similarly, Fig. 8(b) shows that larger Debye lengths also lead to a larger radius of curvature. Furthermore, the motor rotation frequency has a negligible effect on the radius of curvature. In our model, the contour length of the flagellum is set to $\Lambda = 7.5 \mu\text{m}$, consistent with the reported values for *Escherichia coli*⁴⁸. The calculated radii of curvature of the circular motion fall within the range of several to tens of micrometers, which is close to the values observed experimentally^{28,42}.

IV. SUMMARY AND CONCLUSIONS

We simulate the dynamics of a monotrichous bacterium swimming near a solid surface. The bacterium is represented as a chiral two-body model, where hydrodynamic interactions between the flagellum and the surface are neglected. The bacterial state throughout the surface entrapment process is characterized by its height h and inclination angle Ψ . This process is divided into three main stages: approach, reorientation, and surface swimming. Initially, the bacterium swims toward the surface at a velocity proportional to the motor rotation frequency. During the reorientation stage, the cotangent of the inclination angle decays exponentially as a function of the product of the motor rotation frequency and time. The bacterium eventually reaches a stable fixed point (h^*, Ψ^*) determined by the combined effect of the near-field hydrodynamic interactions and the DLVO forces. Finally, the bacterium performs a stable circular motion on the surface. Bacteria with a left-handed flagellum exhibit clockwise circular motion. The radii of curvature of these circular trajectories are primarily determined by the flagellar morphology and the ionic strength of the electrolyte solution, with minimal sensitivity to the zeta potentials of both the cell body and the surface.

These results indicate that the flagellar contour length and motor rotation frequency have a minimal effect on the stable height h^* . However, reducing the ionic strength increases the stable height, which can range from several nanometers up to approximately one hundred nanometers. This may explain the disparity in stable heights observed experimentally for bacteria swimming near solid surfaces. In contrast, the

stable inclination angle depends strongly on both the contour length and ionic strength but is insensitive to the motor rotation frequency. Furthermore, a specific relationship exists between the stable inclination angle, Ψ^* , and the distance, l , between the centers of the cell body and the flagellum, given by $-\cos \Psi^* \propto l^{-2.5}$. Consequently, the stable inclination angle decreases with increasing contour length or decreasing ionic strength. During stable circular motion, both longer flagellar contours and lower ionic strengths lead to larger radii of curvature, r , typically ranging from a few micrometers to tens of micrometers.

ACKNOWLEDGMENTS

We acknowledge computational support from Beijing Computational Science Research Center.

Appendix A: Radius of Curvature of the Circular Trajectory

We derive the formula for the radius of curvature of the bacterial circular motion near a solid surface. The Rodrigues' rotation matrix is given by the following formula^{47,55,56}

$$\mathbf{R}(\hat{\mathbf{e}}, \Delta\varphi) = \cos \Delta\varphi \mathbb{I} + (1 - \cos \Delta\varphi) \hat{\mathbf{e}} \otimes \hat{\mathbf{e}} + \sin \Delta\varphi \hat{\mathbf{e}} \times \approx \mathbb{I} + \Delta\varphi \hat{\mathbf{e}} \times, \quad (\text{A1})$$

where \mathbb{I} is a 3×3 identity matrix, \otimes denotes the Kronecker product, and $(\mathbf{e} \times)$ represents the 3×3 antisymmetric matrix such that $(\mathbf{e} \times) \mathbf{v} = \mathbf{e} \times \mathbf{v}$ for any vector \mathbf{v} . Moreover, $\Delta\varphi = |\mathbf{W}_b| \Delta t$, and $\hat{\mathbf{e}} = \mathbf{W}_b / |\mathbf{W}_b| = (e_x, e_y, e_z)$ is the unit vector along the axis of rotation.

Once the bacterium reaches the stable fixed point (h^*, Ψ^*) , the initial direction of the flagellar axis is given by $\mathbf{e}_1 = (0, \sin \Psi^*, \cos \Psi^*)$. After a time interval Δt , the direction of the flagellar axis becomes

$$\mathbf{e}_2 = \mathbf{R}(\hat{\mathbf{e}}, \Delta\varphi) \mathbf{e}_1 = (e_y \Delta\varphi \cos \Psi^* - e_z \Delta\varphi \sin \Psi^*, \sin \Psi^* - e_x \Delta\varphi \cos \Psi^*, \cos \Psi^* + e_x \Delta\varphi \sin \Psi^*). \quad (\text{A2})$$

At the stable fixed point, the component of the rotational velocity of the cell body along the x -axis is zero, that is, $e_x = 0$. The rotational angle $\Delta\phi$ of the bacterium about the z -axis is defined as the angle between the projections \mathbf{e}_1 and \mathbf{e}_2 onto the xy -plane, given by

$$\begin{aligned} \cos \Delta\phi &= \frac{\sin \Psi^*}{\sqrt{(e_y \Delta\varphi \cos \Psi^* - e_z \Delta\varphi \sin \Psi^*)^2 + \sin^2 \Psi^*}} \\ &= \frac{1}{\sqrt{1 + (e_y \Delta\varphi \cot \Psi^* - e_z \Delta\varphi)^2}}. \end{aligned} \quad (\text{A3})$$

Expanding both sides of the preceding equation using a Taylor series, retaining terms up to the second order, we obtain:

$$1 - \frac{\Delta\phi^2}{2} = 1 - \frac{(e_y \Delta\varphi \cot \Psi^* - e_z \Delta\varphi)^2}{2}. \quad (\text{A4})$$

Therefore, the approximate value of the rotation angle $\Delta\phi$ can be expressed as follows:

$$|\Delta\phi| = |e_y\Delta\phi \cot\Psi^* - e_z\Delta\phi|. \quad (\text{A5})$$

In conjunction with the following relations:

$$\begin{aligned} W_y &= e_y\Delta\phi/\Delta t, \\ W_z &= e_z\Delta\phi/\Delta t. \end{aligned} \quad (\text{A6})$$

The radius of curvature r of the circular motion can be expressed as:

$$r = \frac{U_{\parallel}}{|W_{\perp}|} = \frac{|U_y|}{|W_z - W_y \cot\Psi^*|} \quad (\text{A7})$$

Now, consider the more general case where the direction of the flagellar axis is given by $\mathbf{e}_a =$

$(\sin\Psi^* \cos\phi, \sin\Psi^* \sin\phi, \cos\Psi^*)$. The component of rotational velocity perpendicular to the solid surface, W_{\perp} , can be expressed as:

$$W_{\perp} = W_z - (W_x \cos\phi + W_y \sin\phi) \cot\Psi^*. \quad (\text{A8})$$

Finally, a more general formula for the radius of curvature of the circular trajectory can be expressed as:

$$r = \frac{U_{\parallel}}{|W_{\perp}|} = \frac{\sqrt{U_x^2 + U_y^2}}{|W_z - (W_x \cos\phi + W_y \sin\phi) \cot\Psi^*|} \quad (\text{A9})$$

Appendix B: Resistance Matrix of a Sphere Near a Solid Surface

When the spherical cell body is close to the solid surface, the elements of the resistance matrix of the cell body are⁴²:

$$\frac{Y_{\parallel}^A}{6\pi\mu R_b} = (1.9963\xi - 0.5332) \log\left(\frac{\xi}{\xi+1}\right) + 2.9963 - 0.9689\frac{1}{\xi+1} - 0.5993\frac{1}{(\xi+1)^2} - 0.4691\frac{1}{(\xi+1)^3}, \quad (\text{B1})$$

$$\frac{Y_{\perp}^A}{6\pi\mu R_b} = \frac{2 + 9\xi + 6\xi^2}{2\xi + 6\xi^2}, \quad (\text{B2})$$

$$\frac{Y_{\parallel}^B}{6\pi\mu R_b^2} = (0.4991\xi + 0.1334) \log\left(\frac{\xi}{\xi+1}\right) + 0.4991 - 0.1162\frac{1}{\xi+1} - 0.0165\frac{1}{(\xi+1)^2} + 0.0028\frac{1}{(\xi+1)^3}, \quad (\text{B3})$$

$$\frac{Y_{\parallel}^C}{8\pi\mu R_b^3} = -(0.4 + 0.7898\xi) \log\left(\frac{\xi}{\xi+1}\right) + 0.2101 - 0.0050\frac{1}{\xi+1} - 0.0683\frac{1}{(\xi+1)^2} + 0.2449\frac{1}{(\xi+1)^3}, \quad (\text{B4})$$

$$\frac{Y_{\perp}^C}{8\pi\mu R_b^3} = \left[0.414\xi + 0.318\frac{\xi^2}{\xi+1}\right] \log\left(\frac{\xi}{\xi+1}\right) + 1.732 - 0.684\frac{1}{\xi+1} + 0.037\frac{1}{(\xi+1)^2} + 0.117\frac{1}{(\xi+1)^3}. \quad (\text{B5})$$

where $\xi = h/R_b$, and h is the surface distance between the cell body and the solid surface.

Appendix C: Resistance Matrix of the Flagellum

The bacterium is represented as a chiral two-body model, and the flagellum is simplified to a chiral body, whose motion can be described by a 6×6 resistance matrix⁵²⁻⁵⁴. The detailed expressions for the components of the resistance matrix X_{\parallel}^A , X_{\perp}^A , X_{\parallel}^B , X_{\perp}^B , X_{\parallel}^C and X_{\perp}^C are expressed as follows⁵³:

$$X_{\parallel}^A = \Lambda [k_{\parallel} \cos^2\theta + k_{\perp} \sin^2\theta], \quad (\text{C1})$$

$$X_{\perp}^A = \Lambda \left[k_{\parallel} \frac{\sin^2\theta}{2} + k_{\perp} \frac{1 + \cos^2\theta}{2} \right], \quad (\text{C2})$$

$$X_{\parallel}^B = RL \sin\theta (k_{\perp} - k_{\parallel}), \quad (\text{C3})$$

$$X_{\perp}^B = -\frac{1}{2} RL \sin\theta (k_{\perp} - k_{\parallel}), \quad (\text{C4})$$

$$X_{\parallel}^C = \Lambda R^2 [k_{\parallel} \sin^2\theta + k_{\perp} \cos^2\theta], \quad (\text{C5})$$

$$X_{\perp}^C = \Lambda \left[k_{\perp} \left(\frac{R^2}{2} + \frac{L^2}{12} \right) + (k_{\parallel} - k_{\perp}) \sin^2\theta \left(\frac{R^2}{2\gamma^2} + \frac{L^2}{24} \right) \right]. \quad (\text{C6})$$

where Λ is the contour length, θ is the pitch angle, R is the helix radius, λ is the pitch, $L = \Lambda \cos \theta$ is the axial length, and $\gamma = \tan \theta = 2\pi R/\lambda$. The Gray and Hancock's drag coefficients are^{49,50}:

$$\begin{aligned} k_{\parallel} &= \frac{2\pi\mu}{\ln(2\lambda/a) - 1/2}, \\ k_{\perp} &= \frac{4\pi\mu}{\ln(2\lambda/a) + 1/2}. \end{aligned} \quad (C7)$$

where μ is the dynamic viscosity of the fluid, and a is the filament radius of the flagellum.

- ¹W. R. DiLuzio, L. Turner, M. Mayer, P. Garstecki, D. B. Weibel, H. C. Berg, and G. M. Whitesides, "Escherichia coli swim on the right-hand side," *Nature* **435**, 1271–1274 (2005).
- ²E. Lauga, "Bacterial hydrodynamics," *Annual Review of Fluid Mechanics* **48**, 105–130 (2016).
- ³E. Lauga, M. P. Brenner, and H. A. Stone, "Microfluidics: the no-slip boundary condition," arXiv preprint cond-mat/0501557 (2005).
- ⁴M. Krsmanovic, D. Biswas, H. Ali, A. Kumar, R. Ghosh, and A. K. Dickerson, "Hydrodynamics and surface properties influence biofilm proliferation," *Advances in Colloid and Interface Science* **288**, 102336 (2021).
- ⁵J. W. Costerton, P. S. Stewart, and E. P. Greenberg, "Bacterial biofilms: a common cause of persistent infections," *science* **284**, 1318–1322 (1999).
- ⁶M. Kargar, A. Pruden, and W. A. Ducker, "Preventing bacterial colonization using colloidal crystals," *Journal of Materials Chemistry B* **2**, 5962–5971 (2014).
- ⁷D. van Elsland and J. Neefjes, "Bacterial infections and cancer," *EMBO reports* **19**, e46632 (2018).
- ⁸V. Carniello, B. W. Peterson, H. C. van der Mei, and H. J. Busscher, "Physico-chemistry from initial bacterial adhesion to surface-programmed biofilm growth," *Advances in colloid and interface science* **261**, 1–14 (2018).
- ⁹T. Ghosh, T.-D. Ngo, A. Kumar, C. Ayranci, and T. Tang, "Cleaning carbohydrate impurities from lignin using pseudomonas fluorescens," *Green Chemistry* **21**, 1648–1659 (2019).
- ¹⁰S. Radwan, R. Al-Hasan, S. Salamah, and S. Al-Dabbous, "Bioremediation of oily sea water by bacteria immobilized in biofilms coating macroalgae," *International biodeterioration & biodegradation* **50**, 55–59 (2002).
- ¹¹S. Khalid, A. Gao, G. Wang, P. K. Chu, and H. Wang, "Tuning surface topographies on biomaterials to control bacterial infection," *Biomaterials Science* **8**, 6840–6857 (2020).
- ¹²H. Zhou, G. Dong, G. Gao, R. Du, X. Tang, Y. Ma, and J. Li, "Hydrogel-based stimuli-responsive micromotors for biomedicine," *Cyborg and Bionic Systems* (2022).
- ¹³G. Li and J. X. Tang, "Accumulation of microswimmers near a surface mediated by collision and rotational brownian motion," *Physical review letters* **103**, 078101 (2009).
- ¹⁴A. P. Petroff, X.-L. Wu, and A. Libchaber, "Fast-moving bacteria self-organize into active two-dimensional crystals of rotating cells," *Physical review letters* **114**, 158102 (2015).
- ¹⁵E. Perez Ipiña, S. Otte, R. Pontier-Bres, D. Czerucka, and F. Peruani, "Bacteria display optimal transport near surfaces," *Nature Physics* **15**, 610–615 (2019).
- ¹⁶G. Junot, T. Darnige, A. Lindner, V. A. Martinez, J. Arlt, A. Dawson, W. C. Poon, H. Auradou, and E. Clément, "Run-to-tumble variability controls the surface residence times of e. coli bacteria," *Physical Review Letters* **128**, 248101 (2022).
- ¹⁷D. Giacché, T. Ishikawa, and T. Yamaguchi, "Hydrodynamic entrapment of bacteria swimming near a solid surface," *Physical Review E—Statistical, Nonlinear, and Soft Matter Physics* **82**, 056309 (2010).
- ¹⁸S. E. Spagnolie and E. Lauga, "Hydrodynamics of self-propulsion near a boundary: predictions and accuracy of far-field approximations," *Journal of Fluid Mechanics* **700**, 105–147 (2012).
- ¹⁹M. Molaie, M. Barry, R. Stocker, and J. Sheng, "Failed escape: solid surfaces prevent tumbling of escherichia coli," *Physical review letters* **113**, 068103 (2014).
- ²⁰M. Qi, X. Gong, B. Wu, and G. Zhang, "Landing dynamics of swimming bacteria on a polymeric surface: effect of surface properties," *Langmuir* **33**, 3525–3533 (2017).
- ²¹A. Petroff and A. Libchaber, "Nucleation of rotating crystals by thiovulum majus bacteria," *New Journal of Physics* **20**, 015007 (2018).
- ²²D. Das and E. Lauga, "Transition to bound states for bacteria swimming near surfaces," *Physical Review E* **100**, 043117 (2019).
- ²³Y. Park, Y. Kim, and S. Lim, "Flagellated bacteria swim in circles near a rigid wall," *Physical Review E* **100**, 063112 (2019).
- ²⁴S. Bianchi, F. Saglimbeni, and R. Di Leonardo, "Holographic imaging reveals the mechanism of wall entrapment in swimming bacteria," *Physical Review X* **7**, 011010 (2017).
- ²⁵S. Bianchi, F. Saglimbeni, G. Frangipane, D. Dell'Arciprete, and R. Di Leonardo, "3d dynamics of bacteria wall entrapment at a water–air interface," *Soft matter* **15**, 3397–3406 (2019).
- ²⁶S. M. Mousavi, G. Gompper, and R. G. Winkler, "Wall entrapment of peritrichous bacteria: a mesoscale hydrodynamics simulation study," *Soft Matter* **16**, 4866–4875 (2020).
- ²⁷P. D. Frymier, R. M. Ford, H. C. Berg, and P. T. Cummings, "Three-dimensional tracking of motile bacteria near a solid planar surface," *Proceedings of the National Academy of Sciences* **92**, 6195–6199 (1995).
- ²⁸E. Lauga, W. R. DiLuzio, G. M. Whitesides, and H. A. Stone, "Swimming in circles: motion of bacteria near solid boundaries," *Biophysical journal* **90**, 400–412 (2006).
- ²⁹M. Vigeant and R. M. Ford, "Interactions between motile escherichia coli and glass in media with various ionic strengths, as observed with a three-dimensional-tracking microscope," *Applied and Environmental Microbiology* **63**, 3474–3479 (1997).
- ³⁰J. W. McClaine and R. M. Ford, "Reversal of flagellar rotation is important in initial attachment of escherichia coli to glass in a dynamic system with high- and low-ionic-strength buffers," *Applied and environmental microbiology* **68**, 1280–1289 (2002).
- ³¹M. A.-S. Vigeant, R. M. Ford, M. Wagner, and L. K. Tamm, "Reversible and irreversible adhesion of motile escherichia coli cells analyzed by total internal reflection aqueous fluorescence microscopy," *Applied and environmental microbiology* **68**, 2794–2801 (2002).
- ³²G. Li, L.-K. Tam, and J. X. Tang, "Amplified effect of brownian motion in bacterial near-surface swimming," *Proceedings of the National Academy of Sciences* **105**, 18355–18359 (2008).
- ³³T. Vissers, A. T. Brown, N. Koumakis, A. Dawson, M. Hermes, J. Schwarz-Linek, A. B. Schofield, J. M. French, V. Koutsos, J. Arlt, *et al.*, "Bacteria as living patchy colloids: Phenotypic heterogeneity in surface adhesion," *Science Advances* **4**, eaao1170 (2018).
- ³⁴Y. Shan, L. Liu, Y. Liu, H. Harms, and L. Y. Wick, "Effects of electrokinetic phenomena on bacterial deposition monitored by quartz crystal microbalance with dissipation monitoring," *Environmental science & technology* **54**, 14036–14045 (2020).
- ³⁵P. Sharma and K. H. Rao, "Adhesion of paenibacillus polymyxa on chalcopyrite and pyrite: surface thermodynamics and extended dlvo theory," *Colloids and Surfaces B: Biointerfaces* **29**, 21–38 (2003).
- ³⁶Z. Hong, X. Rong, P. Cai, K. Dai, W. Liang, W. Chen, and Q. Huang, "Initial adhesion of bacillus subtilis on soil minerals as related to their surface properties," *European Journal of Soil Science* **63**, 457–466 (2012).
- ³⁷O. Sipos, K. Nagy, R. Di Leonardo, and P. Galajda, "Hydrodynamic trapping of swimming bacteria by convex walls," *Physical review letters* **114**, 258104 (2015).
- ³⁸H. Shum, E. A. Gaffney, and D. J. Smith, "Modelling bacterial behaviour close to a no-slip plane boundary: the influence of bacterial geometry," *Proceedings of the Royal Society A: Mathematical, Physical and Engineering Sciences* **466**, 1725–1748 (2010).
- ³⁹M. Lavaud, T. Salez, Y. Louyer, and Y. Amarouchene, "Stochastic inference of surface-induced effects using brownian motion," *Physical Review Research* **3**, L032011 (2021).
- ⁴⁰D. Pimponi, M. Chinappi, P. Gualtieri, and C. M. Casciola, "Hydrodynamics of flagellated microswimmers near free-slip interfaces," *Journal of Fluid Mechanics* **789**, 514–533 (2016).
- ⁴¹V. Tokárová, A. Sudalayadum Perumal, M. Nayak, H. Shum, O. Kašpar, K. Rajendran, M. Mohammadi, C. Tremblay, E. A. Gaffney, S. Martel, *et al.*, "Patterns of bacterial motility in microfluidics-confining environments," *Proceedings of the National Academy of Sciences* **118**,

- e2013925118 (2021).
- ⁴²J. Dunstan, G. Mino, E. Clement, and R. Soto, "A two-sphere model for bacteria swimming near solid surfaces," *Physics of Fluids* **24** (2012).
- ⁴³H. Shum and E. A. Gaffney, "Hydrodynamic analysis of flagellated bacteria swimming near one and between two no-slip plane boundaries," *Physical Review E* **91**, 033012 (2015).
- ⁴⁴G. Vizsnyiczai, G. Frangipane, S. Bianchi, F. Saglimbeni, D. Dell'Arciprete, and R. Di Leonardo, "A transition to stable one-dimensional swimming enhances e. coli motility through narrow channels," *Nature communications* **11**, 2340 (2020).
- ⁴⁵E. Lauga and T. R. Powers, "The hydrodynamics of swimming microorganisms," *Reports on progress in physics* **72**, 096601 (2009).
- ⁴⁶B. Liu, L. Chen, and J. Zhang, "Effective and efficient modeling of the hydrodynamics for bacterial flagella," *Physics of Fluids* **37** (2025).
- ⁴⁷B. Liu, L. Chen, and W. Xu, "Effects of flagellar morphology on swimming performance and directional control in microswimmers," *Physics of Fluids* **37**, 041912 (2025).
- ⁴⁸N. C. Darnton, L. Turner, S. Rojevsky, and H. C. Berg, "On torque and tumbling in swimming escherichia coli," *Journal of bacteriology* **189**, 1756–1764 (2007).
- ⁴⁹J. Gray and G. J. Hancock, "The propulsion of sea-urchin spermatozoa," *Journal of Experimental Biology* **32**, 802–814 (1955).
- ⁵⁰A. T. Chwang and T. Y.-T. Wu, "Hydromechanics of low-reynolds-number flow. part 2. singularity method for stokes flows," *Journal of Fluid mechanics* **67**, 787–815 (1975).
- ⁵¹R. Johnson and C. Brokaw, "Flagellar hydrodynamics. a comparison between resistive-force theory and slender-body theory," *Biophysical journal* **25**, 113–127 (1979).
- ⁵²R. Di Leonardo, D. Dell'Arciprete, L. Angelani, and V. Iebba, "Swimming with an image," *Physical review letters* **106**, 038101 (2011).
- ⁵³B. Liu, B. Jin, L. Chen, and N. Liu, "Morphological effects on bacterial brownian motion: Validation of a chiral two-body model," arXiv preprint arXiv:2504.05053 (2025).
- ⁵⁴M. Dvoriashyna and E. Lauga, "Hydrodynamics and direction change of tumbling bacteria," *Plos one* **16**, e0254551 (2021).
- ⁵⁵J. S. Dai, "Euler–rodrigues formula variations, quaternion conjugation and intrinsic connections," *Mechanism and Machine Theory* **92**, 144–152 (2015).
- ⁵⁶R. M. Murray, Z. Li, and S. S. Sastry, *A mathematical introduction to robotic manipulation* (CRC press, 2017).
- ⁵⁷J. A. Redman, S. L. Walker, and M. Elimelech, "Bacterial adhesion and transport in porous media: Role of the secondary energy minimum," *Environmental science & technology* **38**, 1777–1785 (2004).